

## Article

# Combined Terahertz Pulsed Imaging and Optical Coherence Tomography Detection Method for Multiple Defects in Thermal Barrier Coatings

Manting Luo <sup>1,\*</sup>, Shuncong Zhong <sup>2,3</sup>, Yi Huang <sup>2,3</sup>, Zhenghao Zhang <sup>2,3</sup> and Wanli Tu <sup>4</sup><sup>1</sup> School of Mechanical Electrical and Information Engineering, Putian University, Putian 351100, China<sup>2</sup> School of Mechanical Engineering and Automation, Fuzhou University, Fuzhou 350108, China; zhongshuncong@hotmail.com (S.Z.); yihuang@fzu.edu.cn (Y.H.); 200210006@fzu.edu.cn (Z.Z.)<sup>3</sup> Fujian Provincial Key Laboratory of Terahertz Functional Devices and Intelligent Sensing, Fuzhou University, Fuzhou 350108, China<sup>4</sup> Marine Engineering Institute, Jimei University, Xiamen 361021, China; wanlitu@163.com

\* Correspondence: mantingluo163@163.com

**Abstract:** While thermal barrier coatings (TBCs) are being sprayed onto aero-engine turbine blades, or while the engine blade is working, high temperatures and strong impact forces will damage TBCs under thermal cycles, resulting in the coating peeling off from the blades. The current method of using ECT, IRT, or another method alone cannot achieve the real-time detection of coating defects with both high precision and high penetration power. Two detection methods, namely, terahertz pulsed imaging (TPI) and optical coherence tomography (OCT), were combined to evaluate typical defects observed in TBCs (including internal debonding cracks, surface high-temperature cracks, and surface etched cracks). The results showed that the OCT system successfully obtained the micron-level axial resolution, but the detection depth of the OCT system was limited. The TPI system achieved a higher penetration depth than OCT—hence, it can be used for the nondestructive detection and evaluation of the internal debonding defects in the sample—but its resolution needs to be improved. Following this conclusion, a method is proposed using TPI and OCT concurrently for the nondestructive testing and quantitative evaluation of TBCs on etched cracks, thus achieving progress both in terms of depth and resolution. In our experiment, defects with a depth of 519  $\mu\text{m}$  and a width of 100  $\mu\text{m}$  were measured. The proposed method is suitable for situations where multiple defects in TBC samples of blades need to be detected simultaneously during the working process. When there are defects deep inside the sample, more small cracks on the surface can be evaluated to achieve a combination of depth and accuracy.

**Keywords:** thermal barrier coatings; defects detection; terahertz pulsed imaging; optical coherence tomography; depth; resolution



**Citation:** Luo, M.; Zhong, S.; Huang, Y.; Zhang, Z.; Tu, W. Combined Terahertz Pulsed Imaging and Optical Coherence Tomography Detection Method for Multiple Defects in Thermal Barrier Coatings. *Coatings* **2024**, *14*, 380. <https://doi.org/10.3390/coatings14040380>

Academic Editors: Jose Maria De Teresa, Ricardo Lopez Anton and Sion Federico Olive Méndez

Received: 19 February 2024

Revised: 15 March 2024

Accepted: 20 March 2024

Published: 24 March 2024



**Copyright:** © 2024 by the authors. Licensee MDPI, Basel, Switzerland. This article is an open access article distributed under the terms and conditions of the Creative Commons Attribution (CC BY) license (<https://creativecommons.org/licenses/by/4.0/>).

## 1. Introduction

As the core component of the aircraft, the engine works at an internal temperature of more than 1600 °C and even up to 2000 °C during operation [1]. Therefore, the blades of the engine need to be made of special materials, which can withstand high temperatures and high pressure and have good stability. Thermal barrier coatings (TBCs) on the aero-engine turbine blades are an important factor in improving the operating efficiency of the engine [2,3]. As shown in the following picture, Figure 1a is a turbine engine, Figure 1b is the blade of a turbine engine, and the typical structure of the thermal barrier coatings is shown in Figure 1c [4], which consists of super alloy, bond coat (BC), and ceramic layer (Topcoat, TC). The propagation of microcracks on the TC layer and the thickening of thermally grown oxide (TGO) caused by oxidation at high temperatures are the main factors causing the failure of TBCs [5]. At present, the most frequently used method for failure

detection is using a scanning electron microscope (SEM) to obtain the section information of TBCs under static conditions. However, it is a destructive testing method and cannot conduct real-time detection.

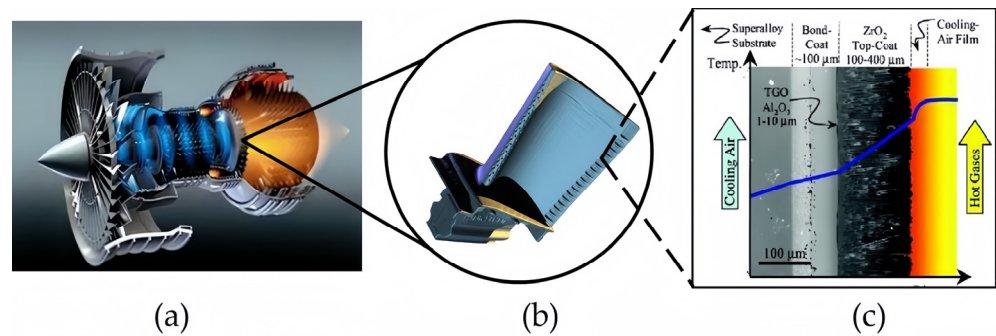


**Figure 1.** Structure of the thermal barrier coating. (a) Turbine engines. (b) Turbine engine blades. (c) Thermal barrier coating structure [4].

Nondestructive techniques for the detection of defects in samples mainly include ultrasonic testing (UT), eddy current testing (ECT), X-ray detection, infrared thermography (IRT), and so on. Among them, ultrasonic testing methods have developed rapidly in recent years. When ultrasound is propagated to the inside of the sample through the coupling agent, the internal defects will hinder its propagation, while the ultrasonic propagation remains unchanged in the position without defects [6,7]. However, it requires contact with the sample at the time of measurement, and the TBCs have many pores, so ultrasonic testing is not suitable for TBCs. Eddy current testing technology mainly detects different eddy current amplitudes and alternating phases generated by different objects moving under the interaction of various alternating phase magnetic fields [8], which is easily affected by material conductivity, sample size, and shape. X-ray detection has the problem of unignored energy radiation; it needs to be isolated and protected when conducting experiments, thus resulting in the limitation of the sample testing environment. At present, the detection resolution of the infrared thermography method needs to be improved, and the penetration ability of samples is insufficient [9–11], so the research on this detection method needs more exploration. Up to now, no nondestructive testing method can fully and accurately detect the characteristics of all TBC systems. Therefore, the advantages of different detection methods should be used for the comprehensive evaluation of TBCs. Li Jianchao et al. [12] reviewed the detection capabilities of different methods of TBC testing, such as UT [7,13], ECT [14], X-ray [15,16], and IRT [17,18]. The detection capabilities of different nondestructive testing TBC methods are summarized in Table 1.

In our work, other two methods were used to evaluate thermal barrier coating defects. The first method was terahertz pulsed imaging (TPI). Terahertz wave is a kind of electromagnetic radiation with a frequency of 0.1~10 THz, which can be used to detect nonpolar objects [19]. TPI has become a new method with great potential in TBC measurement, offering a high signal-to-noise ratio and high detection depth [20]. At present, TPI is used to detect the thickness of TBCs [21], but the thin TGO layer beyond the resolution limit cannot be examined. In terms of pore growth, the tendency for variation in terahertz properties of YSZ ceramic coatings with different microstructure features (porosity, pore-to-crack ratio, pore size) was investigated [22]. The electromagnetic wave transmittance and dielectric properties of thermal barrier coatings, as well as the evolution of defects at the interface of oxide, ceramic, and metal layers [23,24], have been studied, and research is increasingly being devoted to the issues of terahertz peak aliasing and resolution limits that cannot be exceeded. The internal debonding and surface-etched cracks were measured in our experiment to achieve the nondestructive evaluation and prediction of process failure in TBCs. The other method that has been used is optical coherence tomography (OCT), which adopts the principle of near-infrared light interference and can obtain a high resolution

of 5 to 15  $\mu\text{m}$  [25]. Due to significant absorption and strong scattering of near-infrared light in thermal barrier coatings, only surface cracks in thermal barrier coatings can be detected. With its micron-level high resolution, OCT serves as a valuable tool for the auxiliary detection of defects and detailed features in samples. Currently, OCT detection in TBCs primarily focuses on coating thickness and surface defects instead of internal defects [26,27]. This paper proposes a method for the nondestructive testing and quantitative evaluation of thermal barrier coatings by combining TPI and OCT, leveraging the complementary advantages of both techniques. The resolution and penetration depth of these two methods were evaluated to assess their effectiveness.

**Table 1.** Detection ability of different TBCs nondestructive testing methods.

NDT	Detection	Conclusions
UT	Density	Succeeded in evaluating the coating density of varying thicknesses from 0.16 mm to 0.48 mm.
	Thickness	The thickness of YSZ coating (256–330 $\mu\text{m}$ ) sprayed by plasma on the 1Cr18Ni9Ti matrix was measured. The absolute error range between the measurement results and the metallographic observation results is $\pm 10 \mu\text{m}$ , and the relative error range is $\pm 3\%$ .
	Bond quality of TBCs	Could detect 0.2–2.0 mm length of debonding.
ECT	Large internal coating pores, the remaining thickness of the top layer of the ceramic, and its remaining life	Completed the detection of the (1) TC layer with a thickness of 244 $\mu\text{m}$ , with an error of 1.4%; (2) thickness and conductivity of bond coating to detect delamination.
X-ray	Measurement of phase evolution	Studies of phase evolution are performed by X-ray diffraction (XRD) and by evaluating the intensities of a few diffraction peaks for each phase.
	Strain response	Hollow cylindrical specimens, with larger temperature drops across the coating, and significant strain gradients are seen, which can contribute to failure modes occurring within the layer adjacent to the interface.
IRT	Coating thickness	The thickness of nonuniform TBCs was detected, and the results showed that the pulse imaging accuracy was 0.3–2.3 $\mu\text{m}$ .
	Coating defects	Monitors the development of specific failure modes, such as coating delamination after various thermal cycles, utilizing the thermal wave amplitude signals.
	Debonding of samples	Validation tests indicated that blind holes with diameters of 1, 2, and 3 mm and artificial disbonds with diameters of 2 and 3 mm in TBCs are detected.

## 2. Methods and Materials

It is vital to identify engine blade defects as early as possible to prevent the devastating damage caused by aviation accidents. The thermal stress and expansion coefficient differences between the TC on the surface of TBCs and the substrate can lead to thermal stress loss and mismatch in the metal substrate during service. This can result in surface cracks in the TC layer [28], internal debonding, and the growth of a TGO layer, ultimately leading to the failure of the thermal barrier coatings [29].

### 2.1. Methods

The TPI method was first applied in this experiment. When a TPI system is utilized for quantitatively detecting defects in coatings, any defects can lead to changes in the shape of the terahertz detection waveform [30]. As a result, the terahertz method can be employed effectively for the early diagnosis of defects. The terahertz system contains transmission mode and reflection mode, and a diagram of the reflection mode we used in the experiment

is shown in Figure 2a. Figure 2b shows the Terapulse 4000 (TeraView (Cambridge, UK)) we used in this work, where the central wavelength of the laser is 800 nm, and the repetition rate is 80 MHz. The principle of a terahertz system is as follows [31].

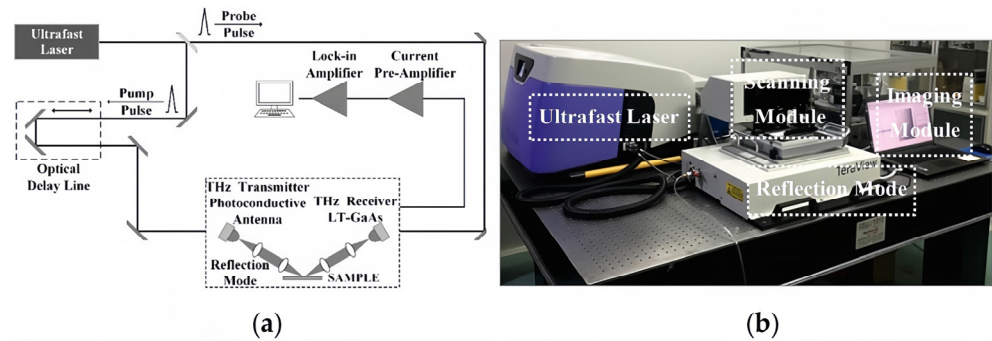


**Figure 2.** TPI system. (a) Diagram of the TPI system [31]. (b) Terapulse 4000 (TeraView) used in the experiment.

By changing the delay of the pump pulse in the terahertz system, the sampling value of the detector changes, and a probe pulse is used to measure the terahertz-induced transient response in the detector. The electric field  $E(t)$  of the terahertz pulse is recorded as a function of the delay time. The information of the electromagnetic pulse  $\tilde{E}(w)$  in the frequency domain can be obtained by the Fourier transform of the time domain pulse, expressed as [32]:

$$\tilde{E}(w) \equiv A(w) \exp[-i\phi(w)] = \int_{-\infty}^{+\infty} E(t) \exp(-iwt) dt, \tag{1}$$

In the equation,  $A(w)$  is the amplitude and  $\phi(w)$  is the phase of the terahertz pulse. Once the electric field of the terahertz pulse is recorded, the Fourier transform can be performed to obtain the amplitude and phase of the pulse. In a system, the time range  $T$  of time-domain waveform measurement is related to the spectral resolution  $\delta_w$  of the terahertz time-domain spectrum, and the time resolution  $\delta_t$  of waveform measurement is related to the spectral range  $\Omega$ . The relationship between them is as follows:

$$\delta_w = 2\pi/T, 2\Omega = 2\pi/\delta_t, \tag{2}$$

The coating thickness can be calculated using the following formula [33]:

$$d_i = c(\Delta t_i - \Delta t_{i-1}) \cos \theta / (2n_{coating}), \tag{3}$$

where  $d_i$  is the thickness of the measured coating ( $i = 1, 2, 3, \dots$ ),  $\Delta t_i$  represents the time delay between the reflection peaks of the TPI detection signals at each coating interface [34], and  $\Delta t_0 = 0$ .  $\cos \theta$  is the cosine of the refraction angle, and because  $\theta = 0^\circ$ ,  $\cos \theta = 1$ .  $n_{coating}$  is the refractive index of the material being measured. In our previous work [23], a signal analysis was carried out on the same sample used in the etched cracks in Section 2.2.3 during SWT processing of the signal, and it was found that the refractive index of the sample concurred with the conclusion that the refractive index of the TC layer of TBCs was 4.7, as established in [35]. Therefore, the refractive index of the TC coating is set as 4.7 in our experiment when calculating the depth of the etched crack.

In addition, detailed information on the structure of the TBC sample can be detected in conjunction with the OCT system. The principle of OCT can be described as “ultrasonic imaging in optics”, which can achieve the tomography of the internal microstructure of a sample. In an OCT system, light from an optical source is split into two paths, a sample path and a reference path. Light in the reference path is reflected from a mirror (RM) whereas light in the sample path is reflected from surface and subsurface features of the ceramic

samples (S). The reflected light from the sample path will only be detected if it travels a distance that closely matches the distance traveled by the light in the reference path—this constraint incorporates depth resolution into the technique [36]. The biggest advantage of the OCT system is that its resolution can reach the micrometer level. The schematic diagram of the OCT system is presented in Figure 3a [37]. Figure 3b is the Ganymede-II (Thorlabs (Newton, NJ, USA)) we used in the work; the central wavelength of the light source is 930 nm, and the axial resolution in the air is 6 μm.

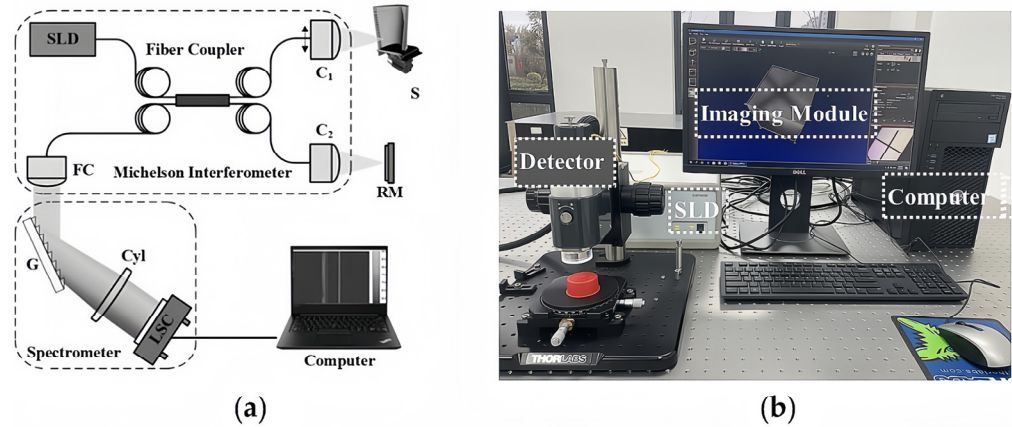


**Figure 3.** (a) Diagram of OCT system [37]. (b) Ganymede-II (Thorlabs) used in the experiment. SLD: super luminescent diode; C1: collimator 1; C2: collimator 2; FC: fiber collimator; S: sample; RM: reference mirror; G: grating; Cyl: cylindrical lens; LSC: linear camera.

When the reference light interferes with the sample light, the OCT system in the frequency domain can obtain complex envelope information in the depth direction of the samples. Among them, the interference light spectrum signal in real form can be represented as [38]:

$$I_{real}(k) = S(k) \left( a_R^2 + 2 \int_{-\infty}^{\infty} a_R a(z) \cos(2knz) dz + \int_{-\infty}^{\infty} \int_{-\infty}^{\infty} a(z) a(z') e^{i2kn(z-z')} dz dz' \right), \quad (4)$$

where  $S(k)$  represents the power spectrum distribution of the light source,  $a_R$  represents the reflection coefficient of the reference mirror,  $a(z)$  represents the reflection or scattering coefficient of the different depth layers of the sample,  $n$  is the refractive index of the sample, and  $k$  is the wave number ( $k = 2\pi/\lambda$ ).  $a(z)$  can be obtained by FFT transformation on the interference spectrum signal  $I_{real}(k)$ .

$$FT^{-1}[I_{real}(k)] = FT^{-1}[S(k)] \otimes \left( a_R^2 \delta(z) + 1/2 a_R a(\hat{z}) + 1/8 AU[a(\hat{z})] \right), \quad (5)$$

where  $a(\hat{z}) = a(z) + a(-z)$ ,  $\otimes$  represents the convolutional operation,  $AU[a(\hat{z})]$  represents the represent autocorrelation function, and the symmetric distribution of  $a(z)$  can be obtained from the above equation  $a(\hat{z})$ , further obtaining  $a(z)$ .

### 2.2. Sample Preparation

Tests were carried out on some samples with thermal barrier coating defects such as internal debonding cracks, surface high-temperature cracks, and surface etched cracks, which often occur in the process of blade work. We describe in detail the preparation process of three different samples, with their ceramic coating being deposited onto components via air plasma spray (APS). The detection target of this experiment was a method that could conveniently detect the occurrence of multiple cracks in the same sample.

### 2.2.1. Internal Debonding Cracks

During the TBC spraying process or while the engine blades are in operation, the difference in thermal expansion coefficients between the TC layer, BC layer, and TGO layer at high temperatures can cause the original bonding effect between the TC and BC layers to transform into thermal mismatch stress, resulting in the detachment of TBCs and exposure of the substrate to high-temperature gases, further causing serious consequences. The production process of the sample with internal debonding cracks in Figure 4 includes three steps. The TBCs are composed of a plasma-sprayed zirconium dioxide ( $ZrO_2$ ) TC layer, BC layer, and nickel-based alloy substrate. The Ni-based alloy substrate size is  $50\text{ mm} \times 40\text{ mm} \times 2\text{ mm}$ , thread through a hole (debonding defect) with a diameter of 2 mm and 3 mm, a base thickness of 5.82 mm, and a TC layer thickness of  $281\text{ }\mu\text{m}$ . First, a threaded hole the size of a TC-BC debonding defect was tapped on the alloy steel, and the matched screw was tightened. Then, the screw head was cut off above the base, and the top surface of the screw was polished. In the following step, mechanical shot peening was carried out on the surface to achieve the preparation of the plastic surface of the component. Finally, the TC layer was sprayed on the upper surface of the component. When the sample had cooled, the screw was loosened to a suitable distance (the distance was smaller than the alloy substrate) to form an air layer to simulate the debonding defects in the sample. As the clearance between the screw and the substrate was small enough to exceed the detection limit of the terahertz pulse, it was regarded as an integral part of the substrate. The sample was prepared with the help of the Beijing Institute of Technology. Figure 4a,b shows the front and backside diagrams of the sample with debonding defects, and Figure 4c is the cross-sectional view of the sample. The two defects are located at different positions on the diagonal of the sample, which makes it convenient to distinguish and coordinate the positioning in the following detection.

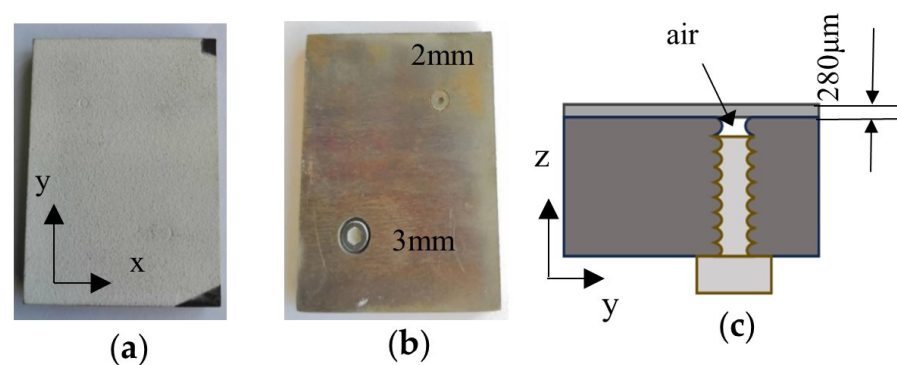


**Figure 4.** Diagram of the TC debonding sample. (a) Front diagram of the sample with debonding defects between TC layer and base. (b) Backside diagram of the sample with debonding defects between TC layer and base. (c) Cross-sectional view of the sample.

### 2.2.2. Surface High-Temperature Cracks

Under the action of working cycles at high temperatures, a large thermal mismatch and corrosion stress exist during service [39]. Due to the phase transition or local sintering of ceramic materials, the surface of the ceramic will shrink. When the internal stress is larger than the limit of the ceramic material, cracks will occur [40]. If the crack area becomes too large, it will cause the ceramic layer to peel off and, thus, greatly reduce the service life. The second type of sample we prepared was a high-temperature oxidation defect sample, a diagram of which is shown in Figure 5a. The production process was as follows (the sample was prepared with the help of the East China University of Science, and we performed the additional heat treatment): The sample was a three-layer structure, including a metal substrate, BC layer, and TC layer. The size of the alloy steel substrate was  $\phi 25 \times 3.1\text{ mm}$ . The ceramic layer material of this sample was yttrium oxide partially stabilized zirconia (8YSZ). The ceramic coating was a powder of  $45\text{--}96\text{ }\mu\text{m}$  in size, and the thickness of the

ceramic coating was about 250–300  $\mu\text{m}$ . The sample was gradually heated to 1100  $^{\circ}\text{C}$  in the heat treatment furnace and held for 40 h of high-temperature oxidation. Then, the sample was cooled in air at a standard pressure from 1100  $^{\circ}\text{C}$  to 10–20  $^{\circ}\text{C}$ . The cooling time was 36 h and the cooling rate was 30  $^{\circ}\text{C}/\text{h}$ . Due to the larger particle size, there was greater stress between the layers, and elongated cracks appeared on the surface of the sample during cooling. The cracks were detected under the metallographic microscope and TPI system in normal environmental circumstances. The holes were discontinuous, and the cracks' size was between 20 and 60  $\mu\text{m}$  as can be seen in the metallographic micrograph in Figure 5b.

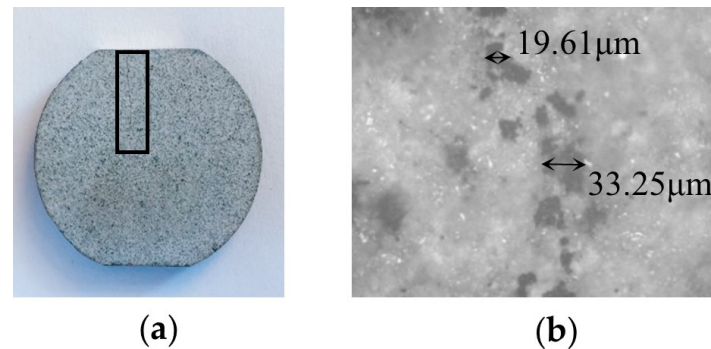


**Figure 5.** A sample with surface high-temperature cracks and its metallographic micrograph. (a) The diagram of the high-temperature oxidation sample, and the box position is the location of the crack. (b) Photographs of cracks under a metallographic microscope.

### 2.2.3. Etched Cracks

The last type of sample contained the etched cracks. The base material of the TBC sample was a nickel-based superalloy block material (brand DZ125) cut into small test pieces (size 30 mm  $\times$  10 mm  $\times$  2 mm) using wire. The metal bonding layer material was nickel-based high-temperature alloy powder. The ceramic layer material was yttrium oxide partially stabilized zirconia (8YSZ). Cracks of different widths and forms were carved on the surface of the TC layer by laser etching to simulate the failure condition of the sample under a strong impact force. This type of damage is usually due to mechanical damage or a sudden impact. Two differently structured TBC samples are shown in Figure 6a,b; the TC layer thickness of sample Figure 6a is about 500  $\mu\text{m}$ , and the TC layer thickness of sample Figure 6b is 265  $\mu\text{m}$ . In the figure, the grooves mark the positions of the samples. The three widths are 100  $\mu\text{m}$ , 200  $\mu\text{m}$ , and 300  $\mu\text{m}$ , respectively, and the depth is 200  $\mu\text{m}$  in all three cases.

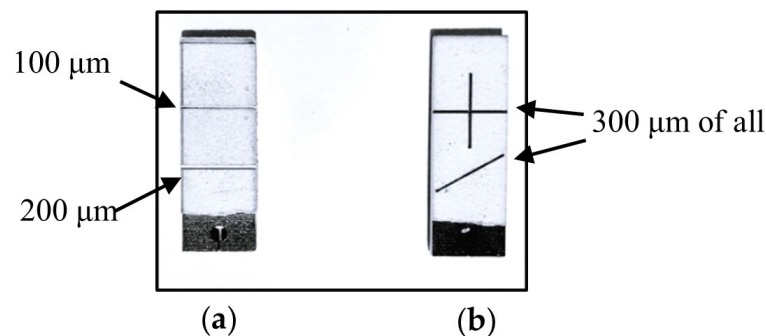


**Figure 6.** Diagram of the etched crack. (a) Sample A with 100  $\mu\text{m}$  and 200  $\mu\text{m}$  width cracks. (b) Sample B with 300  $\mu\text{m}$  width cracks.

### 3. Experiment

TPI and OCT nondestructive testing of different defect samples (such as containing internal debonding cracks, surface high-temperature cracks, and surface etched cracks) were conducted to compare their detection capabilities.

#### 3.1. OCT and TPI Penetration Ability Experiment

##### 3.1.1. Samples without Defects

First, two TBC samples with different TC layer thicknesses were tested under the same spraying conditions on a metal base to evaluate the penetration ability. A frequency-domain OCT system was used to detect the TC layers where the thicknesses were 180  $\mu\text{m}$  and 280  $\mu\text{m}$ . Under the same scanning parameters, the one-dimensional OCT waveforms of the two samples are shown in Figure 7a. Since one-dimensional OCT signals adopt a B-scan in the  $x$ - $z$  direction, the depth information of samples can be obtained directly from images. It can be seen that the penetration capacity of the OCT system for ceramic coatings of different thicknesses is almost the same, but we could not find the difference between the 180  $\mu\text{m}$  and 280  $\mu\text{m}$  samples. In addition, the boundary between the TC and the metal base cannot be detected. This is because the top YSZ of the TBCs is a pore structure, and the SLD light source of OCT has insufficient penetration ability and a strong scattering effect in the pores; hence, the backscattered light that characterizes the sample information collected by the system is weak. Therefore, the detection depth of the OCT system is insufficient.

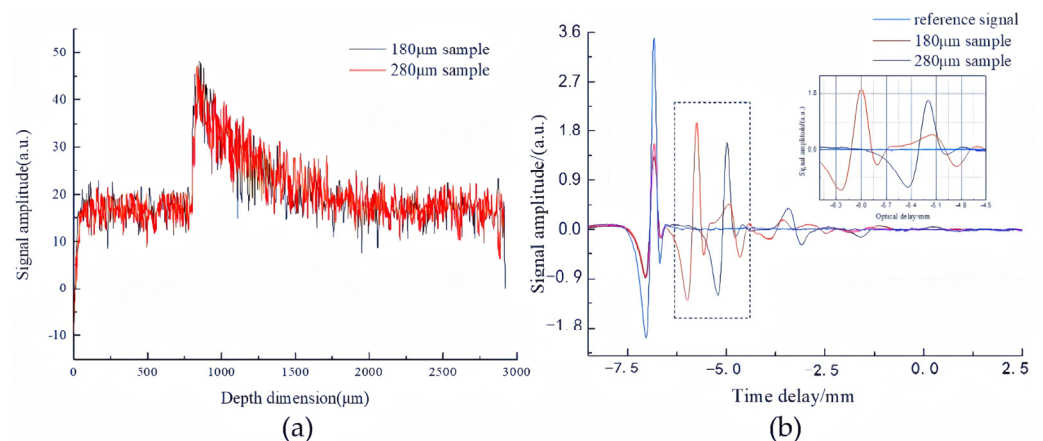


**Figure 7.** (a) One-dimensional waveforms of the sample without defects measured by the OCT system. (b) Time domain pulse signals of 180  $\mu\text{m}$  and 280  $\mu\text{m}$  samples using the TPI system.

The one-dimensional signals of two different coating samples measured using the TPI system are presented in Figure 7b, and the locally amplified signals are shown in the box area. We could see that there is a significant difference in the signals of the two different thickness coatings. The reflection wave of a coating with a thickness of 180  $\mu\text{m}$  occurs earlier than that of 280  $\mu\text{m}$ . The interface stratification can be obtained from the one-dimensional diagram, and thus, we can verify the TC thickness through Formula (3).

The results show that the TPI system has better penetration ability than the OCT system. OCT systems can only detect thermal barrier coatings no thicker than 200  $\mu\text{m}$ , which has been confirmed both in experiments and the literature [36]. The TPI system in this experiment penetrated the thermal barrier coatings above 280  $\mu\text{m}$  and even deeper.

##### 3.1.2. Samples with Internal Debonding Cracks

Furthermore, the debonding defects inside the sample (Figure 4) were prepared to emphasize the penetration ability of the TPI system on the TBCs. As the OCT system could not penetrate the 280  $\mu\text{m}$  TC layer, it was unable to complete the detection of debonding defects.

The TPI two-dimensional C-slice peak-peak imaging of the detected samples is shown in Figure 8a. The outer circular is the shape of the sample table fixture for the TPI system. Occluded by the fixture table, the sample outside the circular shows a black shadow signal under detection. From the two-dimensional image, the position and size of the 2 mm or 3 mm artificial debonding defects can both be observed. We can realize the location of the defects according to the relative position of the fixture table and the sample.

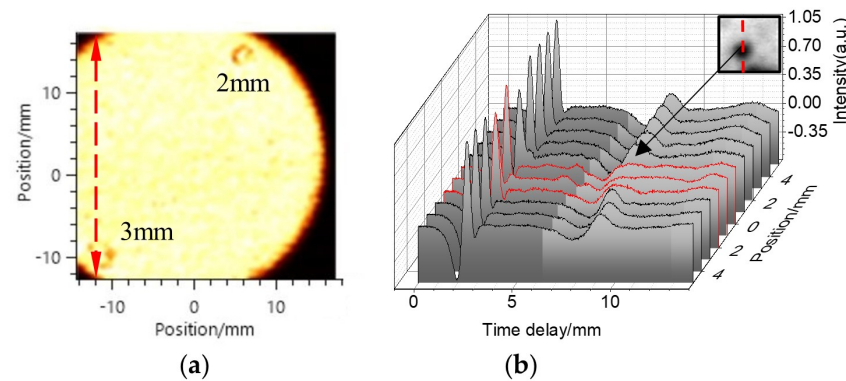


**Figure 8.** (a) Terahertz 2D C-slice peak-peak imaging of debonding defect samples. (b) One-dimensional time-domain waveform of 11 positions in the y-direction of 3 mm defect position.

Terahertz time-domain waveforms of 11 position points in the same x-direction with different y-direction values (dashed line direction in Figure 8a) at the defect location of 3 mm were extracted, and 11 waveform signals were made continuously on the data graph for comparison, as shown in Figure 8b. It can be seen that the position of the debonding defect is also the position of the red terahertz waveform in Figure 8b—the signal has evident deformation, and the peak-to-peak value becomes smaller. In the y-axis position, the deformation waveform can be obtained within the range of the defect size of 3 mm. Due to the small size of the air gap within the defect, the reflected waveforms before and after the air gap at the debonding position cannot be temporally distinguished. The shape of the reflected waveforms differs from the original incident waveforms, indicating the presence of defects after the terahertz wave passes through the detected object.

It can be concluded that the TPI system can realize the quantitative detection of the debonding defects even inside the sample with a diameter larger than 2 mm, and we can distinguish both 2 mm and 3 mm defect locations in the image. Hence, it was confirmed here once again that terahertz waves have a stronger penetration ability than infrared light sources in OCT systems.

### 3.2. Resolution Ability Experiment of OCT and TPI

#### 3.2.1. Surface High-Temperature Cracks

In this experiment, high-temperature oxidation defects on the surface of the sample (Figure 5) were detected to test the resolution of the OCT system.

Three-dimensional imaging was used to analyze more detailed information. As shown in Figure 9a, the red box is the sample detection range. It is not appropriate to set the scanning range to be too large concurrently with a small step size; otherwise, the storage memory will overflow. We set the detection range as  $0.6 \text{ mm} \times 1.12 \text{ mm} \times 1.5 \text{ mm}$  in the experiment; the detection resolution was  $2 \mu\text{m} \times 2 \mu\text{m} \times 2.04 \mu\text{m}$ ; the acquisition time (3D) was about 3 min; and the data storage and imaging time was about 2 min. Figure 9b is the x–y section diagram near the focal point of the 3D OCT image of the sample, and the approximate position and width of the crack can be seen in the white arrow and square in the figure. Due to the existence of an air gap at the crack location, the refractive index is lower than that of other coating components, so the color of the position indicated is dark and its backscattered light is weak. Figure 9c is the cross-section of the y–z axis of the volume standard imaging. It can be seen that the crack location also presents a low

backscattering region different from the normal location in the depth direction. In the figure, the depth of the crack can be evaluated according to the coordinates of defects in the  $z$ -direction. Therefore, combining with the sample signals of different sections, the location and quantification of sample cracks can be realized. The crack width of this sample is about  $35\ \mu\text{m}$ .

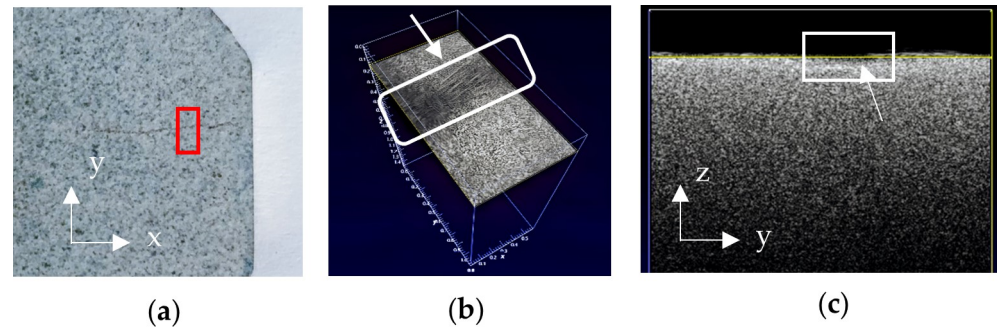


**Figure 9.** Scanning images of high-temperature oxidation cracks. (a) The picture of the high-temperature oxidation crack on the OCT sample table; the red box is the scanning area of the picture. (b)  $x$ - $y$  cross-section near the focal point of 3D OCT imaging of the sample. (c)  $y$ - $z$  cross-section of a location for volume standard OCT imaging of the sample.

There are no TPI images as the resolution is insufficient to produce worthwhile measurements. The main reason is that the terahertz beam after collimation is above  $100\ \mu\text{m}$ , which limits the lateral resolution of the TPI system. As the OCT system has a higher detection resolution, it can obtain better results in shallow surface imaging, thus showing its advantages. On the other hand, to collect more detailed information, the OCT system needs to set a shorter scanning step and collect more sample data points, which may take more time. Therefore, OCT is more suitable to be an auxiliary means of detecting TBC samples.

### 3.2.2. Etched Cracks

The mechanical damage cracks were simulated by creating artificial etched cracks (Figure 6), and then, both systems were simultaneously used to detect them. First, the sample was detected by TPI, with the detection range of the system set as  $14\ \text{mm} \times 14\ \text{mm}$  and  $18\ \text{mm} \times 10\ \text{mm}$ , the scanning step as  $200\ \mu\text{m}$ , and the detection time as 5 min.

The size and location of the  $100$ – $300\ \mu\text{m}$  crack can be obtained from the TPI two-dimensional C-slice diagram in Figure 10.

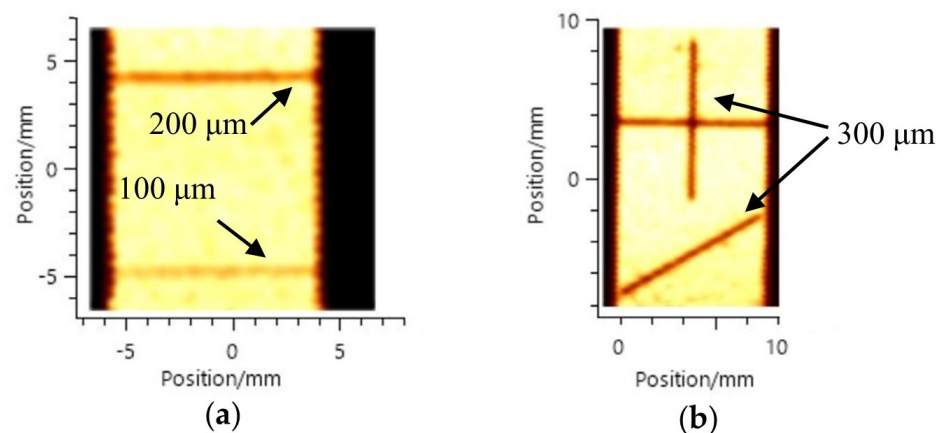


**Figure 10.** Diagram of two samples with surface cracks etched in different directions and widths. (a) Two-dimensional imaging of TBCs with horizontal cracks etched: the two cracks etched are  $100\ \mu\text{m}$  and  $200\ \mu\text{m}$ . (b) Two-dimensional imaging of TBCs with mixed direction cracks etched: all cracks etched were  $300\ \mu\text{m}$ .

One-dimensional waveforms were also extracted from the surface crack data of 100  $\mu\text{m}$  and 200  $\mu\text{m}$  in Figure 10a, and then, the waveform changes were compared in Figure 11a. It can be seen from the figure that the larger the defect width, the smaller the TPI signal strength. When the width of the defect is 200  $\mu\text{m}$ , the surface reflection terahertz time-domain signal of the crack is at its weakest. The terahertz waves are scattered within the groove of the etched crack, resulting in a decrease in the returned terahertz intensity. At the same time, with the increase in the width of the defect, the waveform shifted backward and deformed. When the width of the defect was 200  $\mu\text{m}$ , a second terahertz reflection peak appeared, and the depth of the artificial crack could be calculated as 266  $\mu\text{m}$  according to the flight time of the two terahertz reflection peaks. However, when the defect width is 100  $\mu\text{m}$ , it is quite difficult to distinguish the waveform change in the defect due to the resolution limit of the TPI system and the superimposed terahertz waveform. In addition, we observed that the reflection peak in the dashed elliptical box was the bottom of the TC layer, and the thickness of the TC layer was 519  $\mu\text{m}$ , which was consistent with the sample parameters. Then, we performed a spectrum transformation for one-dimensional signals at different positions with different widths, as shown in Figure 11b. The defect information of the sample can be obtained when observing only the magnitude of the electric field in the frequency domain. The frequency domain electric field intensity at 100  $\mu\text{m}$  is slightly decreased and barely recognizable, and when the defect size reaches 200  $\mu\text{m}$ , the spectral absorption peak caused by the defect structure is quite significant. The frequency at which the minimum intensity is located indicates the corresponding defect width.

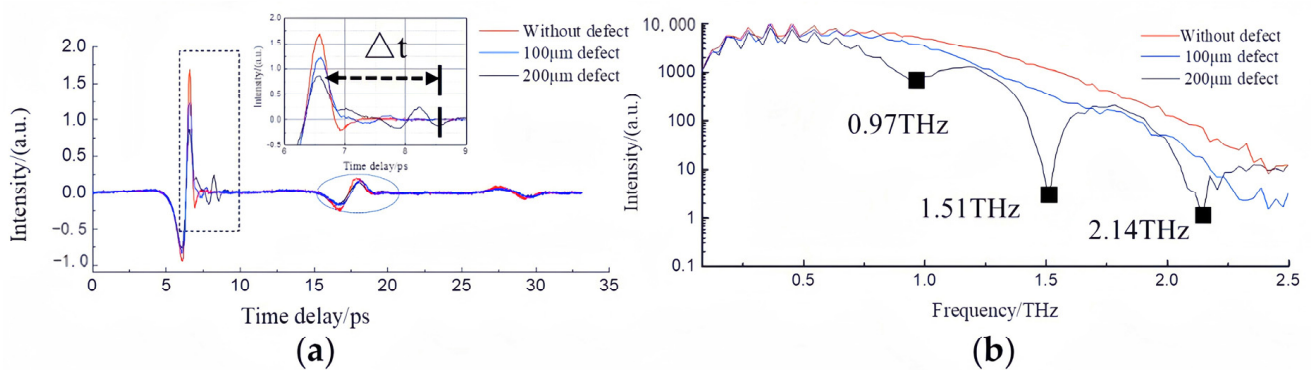


**Figure 11.** (a) One-dimensional time-domain signals for the positions without defects and signals for the positions of etched cracks with different widths. (b) One-dimensional frequency-domain signal of etching crack positions without defects and with different defect widths.

It can be seen from the one-dimensional time-domain/frequency-domain waveform and two-dimensional image of the sample that the TPI system can easily realize the detection of laser etching cracks on the surface of about 200  $\mu\text{m}$  width.

The B-slice cross-sectional diagrams (with and without defects) at different positions of the 300  $\mu\text{m}$  defect (“+” shape) sample in Figure 10b are compared as follows (Figure 12). The  $x$ -coordinate is the scanning position of the high-precision linear platform, and the  $y$ -coordinate is the optical delay line of the system. It can be seen from Figure 12b that in the depth direction, there is an extra reflection interface. In a partially enlarged image in Figure 12b, the terahertz reflection wave at the bottom of the etched crack is represented by the arrow at position 1. In addition, TPI can simultaneously detect the total thickness of the TC layer (arrow 2).

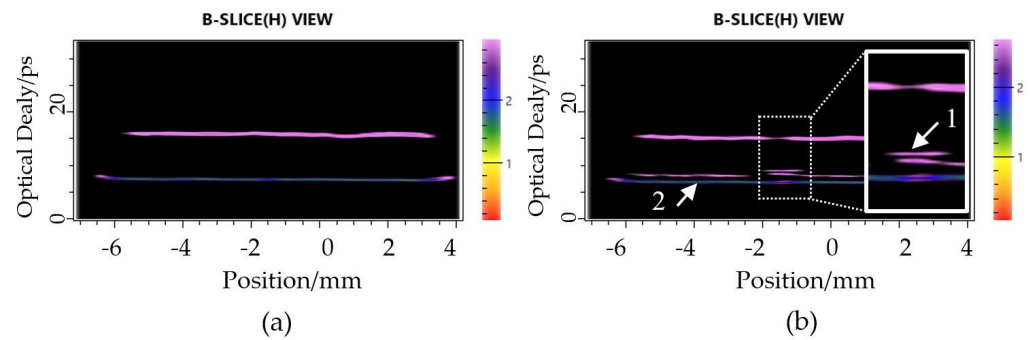


**Figure 12.** B-slice cross-sectional imaging of normal and defective locations on the etched crack sample. (a) B-slice cross-sectional imaging of the normal location on the etched crack sample. (b) B-slice cross-sectional imaging of the defect location on the etched crack sample.

The OCT system was also used to detect the surface “+”-shaped etched crack samples (Figure 6b), and the detection range and accuracy were compared with TPI. As mentioned before, the crack width was about  $300\ \mu\text{m}$ . The detection range was set to  $1.5\ \text{mm} \times 1.7\ \text{mm} \times 1.5\ \text{mm}$ , with a detecting resolution of  $3\ \mu\text{m} \times 3\ \mu\text{m} \times 2\ \mu\text{m}$ . The imaging time (3D) was about 3 min. The sample pictures and OCT detection results are shown in Figure 13. Figure 13a is the actual photo of the sample, and the red area indicates the scan range. When the area becomes larger, the data points become larger, thereby increasing the imaging workload. Figure 13b is the three-dimensional OCT imaging of the sample (surface imaging only), from which the width and depth of the manufactured crack can be seen, and circular grooves formed by repeated etching can be seen at the intersection of the two crack centers, as indicated by the white circle and arrow marks in the figure, which are not detectable in TPI imaging. Figure 13c is the volume standard imaging, in which the three-dimensional structure information of the sample can be seen more intuitively and reliably. The black part of the surface in the image is the etched crack. Figure 13d is the  $x$ - $z$  direction of the volume standard imaging where the bottom of the sample groove has stronger interfacial reflection than the air, which represents the depth information of the sample groove. We can achieve the depth information of the surface crack, as indicated by the distance  $d$  shown in Figure 13d.

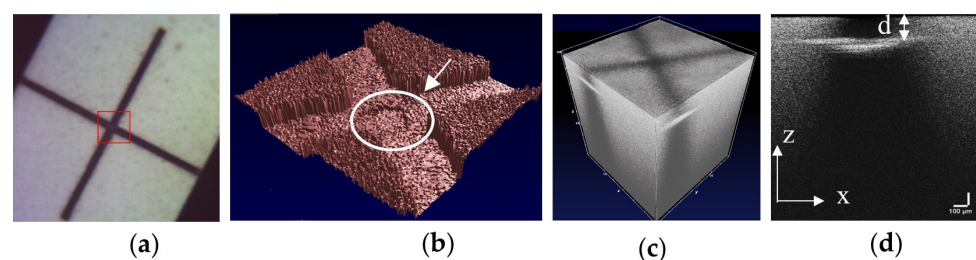


**Figure 13.** (a) The picture of the surface etched crack on the OCT sample table; the red box is the scanning area of the picture. (b) 3D OCT imaging of the sample (surface imaging only). (c) Volume standard imaging of the sample. (d) An  $x$ - $z$  cross-section of a  $300\ \mu\text{m}$  etched crack at a certain location.

Furthermore, Figure 14a shows the one-dimensional TPI signals of the  $300\ \mu\text{m}$  etched crack, and Figure 14b shows the OCT detection signals of the same crack.

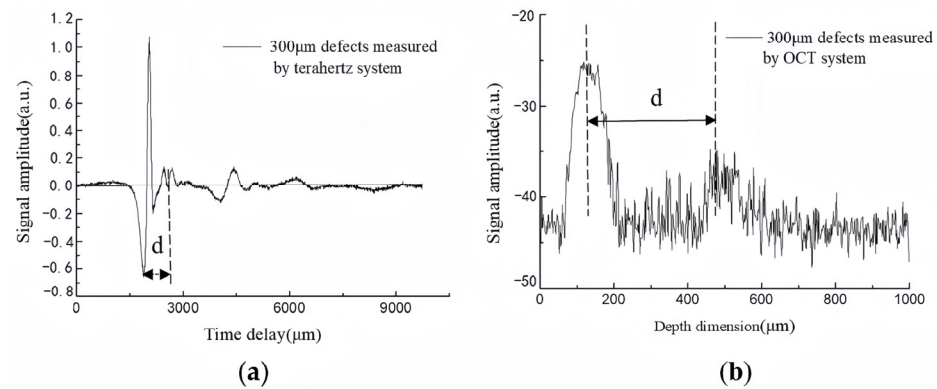


**Figure 14.** TPI one-dimensional signal and OCT one-dimensional signal of surface etched “+”-shaped crack samples. (a) TPI signals of etched cracks. (b) OCT signals of etched cracks.

As can be seen from the figure, although the light intensities of the two signals are quite different from each other, the one-dimensional signals of both show the reflected crest position of light waves at the layered interface of the sample. The distance  $d$  of the interface can be obtained, being the depth of the defect. In addition, the waveform and the peak characteristics of the two figures are quite different. As can be seen, the TPI signals have stronger signal intensity with a better signal-to-noise ratio and smoother waveform. The detected TPI signals reveal multiple reflection echoes between the interlayer boundaries of the sample, suggesting penetration through ceramic coating samples of significant thickness beyond the metal bond coat layer and substrate. However, in the one-dimensional OCT image, the backscattered signal intensity from detectors appears weaker, with insufficient depth of penetration due to the strong scattering effect of the ultra-radiant light source in the ceramic gap and its relatively weak intensity.

Last, the widths of the defects at 100  $\mu\text{m}$  and 200  $\mu\text{m}$ , measured using TPI, OCT, and metallographic microscopy, are compared in Table 2. The width of each defect was measured three times, and the average value was obtained. One of the reasons considered to explain the measurement error of the crack width in both OCT and TPI systems is the error in setting the refractive index of the TC layer. Due to the influence of different spraying conditions and structural parameters on the refractive index of TBCs, the optical path length ( $nd$ ) can be used to verify the measurement accuracy of the samples when comparing OCT and TPI results.

**Table 2.** Mean thickness comparison of TPI, OCT, and MM <sup>1</sup>.

	Resolution	Thickness of the TC Layer	Crack 1# Width (100 $\mu\text{m}$ )	Crack 2# Width (200 $\mu\text{m}$ )	Characteristic of Method
TPI	~100 $\mu\text{m}$ (lateral) 30 $\mu\text{m}$ (axial)	519 $\mu\text{m}$	Hard to detect	253 $\mu\text{m}$	Real-time, nondestructive
OCT	5–15 $\mu\text{m}$ (axial)	Not detected	121 $\mu\text{m}$	244 $\mu\text{m}$	Real-time, nondestructive
MM	0.2–0.5 $\mu\text{m}$	Need to be cut and polished	115 $\mu\text{m}$	221 $\mu\text{m}$	Damaged, in vitro

<sup>1</sup> MM: Metallographic microscope.

The results showed a good resolution advantage of using the OCT system because it is closer to achieving the measurement results of a metallographic microscope, which has the highest resolution. When the defect width is 100  $\mu\text{m}$ , the relative error between the two methods is 5%, and when the defect width is 200  $\mu\text{m}$ , the relative error is 10%. However, the disadvantage is that we cannot detect the bottom of the TC layer, that is, we cannot know the actual thickness of the TC layer.

We further analyzed the width of defects measured by TPI, OCT, and MM methods at 100  $\mu\text{m}$ , 200  $\mu\text{m}$ , and 300  $\mu\text{m}$  (see Figure 15).

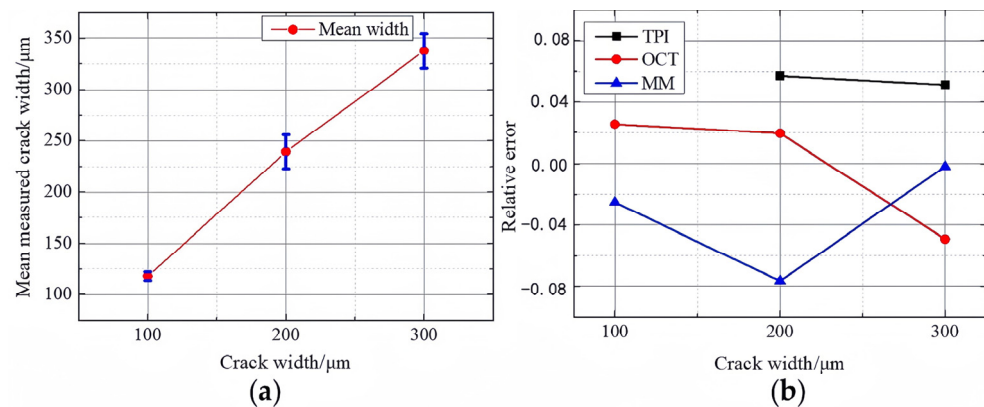


**Figure 15.** (a) The mean value and standard deviation of width measurements using three methods for detecting defects at 100  $\mu\text{m}$ , 200  $\mu\text{m}$ , and 300  $\mu\text{m}$ . (b) The relative errors of TPI, OCT, and MM methods for measuring defects at 100  $\mu\text{m}$ , 200  $\mu\text{m}$ , and 300  $\mu\text{m}$  with respect to the mean values.

The mean value and standard deviation of three methods for detecting the width of three defects were calculated as shown in Figure 15a. The average values were 118  $\mu\text{m}$ , 239  $\mu\text{m}$ , and 337  $\mu\text{m}$ , respectively. The minimum standard deviation is 4.2  $\mu\text{m}$  when measuring 100  $\mu\text{m}$  defects. Figure 15b shows the relative errors of TPI, OCT, and MM methods for measuring defects at 100  $\mu\text{m}$ , 200  $\mu\text{m}$ , and 300  $\mu\text{m}$  with respect to the mean values. (The TPI method's values of 100  $\mu\text{m}$  cracks were omitted because they could not be detected). The results measured by OCT and MM are closer to the mean value of the three methods; however, due to the higher resolution of the MM method, we still used the measurement results of MM as a reference value in this experiment. In addition, the resolution provided by OCT is higher than that of TPI, whose detection value is closer to the MM method and its mean value.

In conclusion, OCT signals can detect the repeated etched grooves at defect intersections and complete the 100  $\mu\text{m}$  defect detection in this experiment on etched cracks. This demonstrated a higher detection accuracy, and thus, it was superior when the crack depth was shallower. The experiments show that the scanning range of OCT is limited compared with TPI, and the data storage is more complex. Defect measurement can be accomplished at the micron level, but the detection depth is insufficient. TPI obtained the width and depth of the 200  $\mu\text{m}$  crack, as well as the total thickness of the TC layer (about 519  $\mu\text{m}$ ), which is conducive to our assessment of the remaining life of the blade. For the 100  $\mu\text{m}$  surface crack, we need to use OCT as a detail supplement, the resolution of which facilitates detection down to the 10  $\mu\text{m}$  level.

#### 4. Conclusions

The above experiments completed the detailed evaluation of the debonding defects, high-temperature oxidation cracks, and etched cracks on the TBCs by TPI and OCT systems.

- (1) A TPI system was used to detect the typical defects of the TBCs, such as debonding defects and etched cracks. It was verified that the size of debonding defects larger than 2 mm and the etched defects above 200  $\mu\text{m}$  could achieve good qualitative and quantitative measurement results (100  $\mu\text{m}$  defect can be hard to obtain). It was also verified that the thickness of the penetrable TC layer exceeds 500  $\mu\text{m}$ . However, the detection of high-temperature oxide cracks by TPI failed because of the resolution limitation of TPI.
- (2) The typical defects of TBCs (surface etched cracks and high-temperature oxidation cracks) were evaluated by the OCT system. The results show that the high-temperature oxidation cracks can be detected by OCT with short coherence length and higher resolution, and the repeated etched circular pits of surface etched cracks can be observed better than by the TPI system. OCT can also easily measure the width and depth of etched cracks on 100  $\mu\text{m}$  surfaces, with a relative error of only

5%. The high precision measurement of OCT systems complements the TPI detection information characteristics, but it can only complete the shallow surface crack measurement. This conclusion is demonstrated objectively by comparing the one-dimensional time-domain signal of terahertz with the one-dimensional time-domain signal of OCT.

Overall, OCT can detect etched defects with a width as small as 100  $\mu\text{m}$  (even high-temperature oxidation cracks of about 35  $\mu\text{m}$  can be seen), and TPI can detect TC layers with a thickness of more than 500  $\mu\text{m}$ . Thus, it is concluded that the TPI method can achieve a larger detection depth, while the OCT system can improve the detection resolution at the expense of its penetration depth in the sample. When the same TBC sample is working and produces various types of defects, OCT can be used to measure the small surface defects of the sample, while TPI can measure the internal defects. The two methods can be comprehensively used in TBC defect measurement, which presents the opportunity to obtain more sample information and makes it easier to monitor and comprehensively evaluate TBC faults in a timely manner. We may evaluate more small cracks on the surface when there are also defects in deeper areas inside the sample. This will result in a higher resolution and better depth information than using UT or ECT alone (can detect the thickness of about 200  $\mu\text{m}$  of TC layer). In general, it enriches the measuring means and possibilities of TBCs. Our ongoing work is focused on investigating the fusion of TPI and OCT images of the same sample to provide more intuitive information.

**Author Contributions:** Conceptualization, M.L. and S.Z.; methodology, M.L. and S.Z.; software, M.L.; validation, M.L. and Y.H.; formal analysis, M.L.; investigation, M.L. and Z.Z.; resources, M.L. and Y.H.; data curation, M.L. and Z.Z.; writing—original draft preparation, M.L.; writing—review and editing, M.L., S.Z. and W.T.; project administration, M.L., S.Z. and W.T.; funding acquisition, M.L. and S.Z. All authors have read and agreed to the published version of the manuscript.

**Funding:** This research was funded by the Youth Fund of the National Natural Science Foundation of China, grant number 52101355; the Youth Fund of the Fujian Provincial Natural Science Foundation, grant number 2022J05256; Fujian Provincial Natural Science Foundation, grant number 2022J01116; Fujian Province science and technology innovation key research and industrialization projects, grant number 2023XQ017; and the Open Project of Fujian Provincial Key Laboratory of Terahertz Functional Devices and Intelligent Sensing, grant number FPKLTFDIS202305.

**Institutional Review Board Statement:** Not applicable.

**Informed Consent Statement:** Not applicable.

**Data Availability Statement:** Data are contained within the article.

**Acknowledgments:** We thank the East China University of Science and Technology and Beijing Institute of Technology for providing the experimental samples. We also thank Walter Nsengiyumva for his suggestions and revisions to the article.

**Conflicts of Interest:** The authors declare no conflicts of interest.

## References

1. Wen, F.J.; Long, Z.; Xing, Z.G.; Guo, W.L.; Huang, Y.F. Research on Damage Behavior of Thermal Barrier Coatings Based on Acoustic Emission Technology. *Nondestruct. Test. Eval.* **2023**, *38*, 67–89. [[CrossRef](#)]
2. Sun, F.S.; Fan, M.B.; Cao, B.H.; Zheng, D.D.; Liu, H.; Liu, L. Terahertz Based Thickness Measurement of Thermal Barrier Coatings Using Long Short-Term Memory Networks and Local Extrema. *IEEE Trans. Ind. Inform.* **2022**, *18*, 2508–2517. [[CrossRef](#)]
3. Ye, D.D.; Wang, W.Z.; Zhou, H.T.; Fang, H.J.; Huang, J.B.; Li, Y.J.; Gong, H.H.; Li, Z. Characterization of Thermal Barrier Coatings Microstructural Features Using Terahertz Spectroscopy. *Surf. Coat. Technol.* **2020**, *394*, 125836–125846. [[CrossRef](#)]
4. Zhang, Z.H.; Huang, Y.; Zhong, S.C.; Lin, T.L.; Zhong, Y.J.; Zeng, Q.M.; Nsengiyumva, W.; Yu, Y.J.; Peng, Z.K. Time of Flight Improved Thermally Grown Oxide Thickness Measurement with Terahertz Spectroscopy. *Front. Mech. Eng.* **2022**, *17*, 49–61. [[CrossRef](#)]
5. Sun, F.Z.; Cao, B.H.; Fan, M.B.; Liu, L. Physics-Based Deep Learning Framework for Terahertz Thickness Measurement of Thermal Barrier Coatings. *SSRN Electron. J.* **2023**, *in press*. [[CrossRef](#)]

6. Martin, E.; Larato, C.; Clément, A.; Saint-Paul, M. Detection of delaminations in sub-wavelength thick multi-layered packages from the local temporal coherence of ultrasonic signals. *NDT E Int.* **2008**, *41*, 280–291. [[CrossRef](#)]
7. Zhang, X.; Augereau, F.; Laux, D.; Le Clezio, E.; Ismaili, N.A.; Kuntz, M.; Despau, G. Non-destructive Testing of Paint Coatings on Steel Plates by Ultrasonic Reflectometry. *J. Nondestruct. Eval.* **2014**, *33*, 504–514. [[CrossRef](#)]
8. Tu, W.L.; Zhong, S.C.; Xu, Y.Q. Terahertz Quantitative Nondestructive Evaluation of Marine Protective Coating. *Ship Eng.* **2017**, *02*, 79–85.
9. He, Y.Z.; Tian, G.Y.; Pan, M.C.; Chen, D.X.; Zhang, H. An Investigation into Eddy Current Pulsed Thermography for Detection of Corrosion Blister. *Corros. Sci.* **2014**, *78*, 1–6. [[CrossRef](#)]
10. Dong, L.H.; Guo, W.; Wang, H.D.; Xing, Z.G.; Feng, F.Z.; Wang, B.Z.; Gao, Z.F. Inspection of interface debonding in thermal barrier coatings using pulsed thermography. *Ac-Ta Aeronaut. Et Astronaut. Sin.* **2019**, *40*, 288–297.
11. Liu, Z.W.; Jiao, D.C.; Shi, W.X.; Xie, H.M. Linear Laser Fast Scanning Thermography NDT for Artificial Disbond Defects in Thermal Barrier Coatings. *Opt. Express* **2017**, *25*, 31789–31800. [[CrossRef](#)] [[PubMed](#)]
12. Li, J.C.; He, Q.; Lv, Y.F.; Liang, L.K. Research Progress on Non-destructive Testing Method of Thermal Barrier Coatings. *China Surf. Eng.* **2019**, *32*, 16–26.
13. Ma, Z.Y.; Zhao, Y.; Luo, Z.B.; Lin, L. Ultrasonic Characterization of Thermally Grown Oxide in Thermal Barrier Coating by Reflection Coefficient Amplitude Spectrum. *Ultrasonics* **2014**, *54*, 1005–1009. [[CrossRef](#)]
14. Li, Y.; Chen, Z.M.; Mao, Y.; Qi, Y. Quantitative Evaluation of Thermal Barrier Coating Based on Eddy Current Technique. *NDT E Int. Independ. Nondestruct. Test. Eval.* **2012**, *50*, 29–35.
15. Grégoire, W.; Shklover, V.; Steurer, W.; Bachegowda, S.; Bossmann, H.P. Phase Evolution in Yttria-Stabilized Zirconia Thermal Barrier Coatings Studied by Rietveld Refinement of X-Ray Powder Diffraction Patterns. *J. Am. Ceram. Soc.* **2010**, *90*, 2935–2940.
16. Knipe, K.; Manero, A.; Siddiqui, S.F.; Meid, C.; Wischek, J.; Okasinski, J.; Almer, J.; Karlsson, A.M.; Bartsch, M.; Raghavan, S. Strain response of thermal barrier coatings captured under extreme engine environments through synchrotron X-ray diffraction. *Nat. Commun.* **2014**, *5*, 4559–4565. [[CrossRef](#)] [[PubMed](#)]
17. Tang, Q.J.; Dai, J.M.; Liu, J.Y.; Liu, C.S.; Liu, Y.L.; Ren, C.P. Quantitative Detection of Defects Based on Markov-PCA-BP Algorithm Using Pulsed Infrared Thermography Technology. *Infrared Phys. Technol.* **2016**, *77*, 144–148. [[CrossRef](#)]
18. Newaz, G.; Chen, X.Q. Progressive Damage Assessment in Thermal Barrier Coatings Using Thermal Wave Imaging Technique. *Surf. Coat. Technol.* **2005**, *190*, 7–14. [[CrossRef](#)]
19. Sterczewski, L.A.; Westberg, J.; Yang, Y.; Burghoff, D.; Reno, J.; Hu, Q.; Wysocki, G. Terahertz hyperspectral imaging with dual chip-scale combs. *Optica* **2019**, *6*, 766. [[CrossRef](#)]
20. Cao, B.H.; Li, H.X.; Fan, M.B.; Sun, F.S.; Ye, B. Model-Driven Terahertz Image Reconstruction Method for Debonding Defects in Thermal Barrier Coatings. *Appl. Opt.* **2023**, *62*, 9343–9352. [[CrossRef](#)]
21. Zhong, S.C. Progress in Terahertz Nondestructive Testing: A review. *Front. Mech. Eng.* **2019**, *14*, 273–281. [[CrossRef](#)]
22. Liu, Z.H.; Man, R.X.; Wang, K.X.; Wu, Y.H. Nondestructive Evaluation of Coating Defects and Uniformity Based on Terahertz Time-Domain Spectroscopy. *Mater. Eval.* **2022**, *80*, 34–43. [[CrossRef](#)]
23. Luo, M.T.; Zhong, S.C.; Yao, L.G.; Tu, W.L.; Chen, W.Q. Thin Thermally Grown Oxide Thickness Detection In thermal Barrier Coatings Based on SWT-BP Neural network Algorithm and Terahertz Technology. *Appl. Opt.* **2020**, *59*, 4097–4104. [[CrossRef](#)] [[PubMed](#)]
24. Xu, Y.F.; Wang, X.Y.; Zhong, S.C.; Zhang, L.Y.; Chen, X.F. Location and Separation of Terahertz Echo Signal of TBCs Based on Sparse Representation Method. *J. Mech. Eng.* **2023**, *59*, 9–19.
25. Huang, D.; Swanson, E.A.; Lin, C.P.; Schuman, J.S.; Stinson, W.G.; Chang, W.; Hee, M.R.; Flotte, T.; Gregory, K.W.; Puliafito, C.A.; et al. Optical Coherence Tomography. *Science* **1991**, *254*, 1178–1181. [[CrossRef](#)] [[PubMed](#)]
26. Ellingson, W.A.; Lipanovich, R.; Hopson, S.; Visher, R. Nondestructive Evaluation Methods for High Temperature Ceramic Coatings. *Ceram. Eng. Sci. Proc.* **2006**, *3*, 207–214.
27. Alsayed, E.Z.; Sadr, A.; Nakashima, S.; Hariri, I. Demineralization Prevention by Enamel Resin Coating: Optical Coherence Tomography Evaluation. In Proceedings of the IADR/AADR/CADR General Session and Exhibition 2013, Seattle, DC, USA, 23 March 2013.
28. Bochenek, K.; Wglewski, W.; Strojny-Ndza, A.; Pietrzak, K.; Chmielewski, T.; Chmielewski, M.; Basista, M. Microstructure, Mechanical, and Wear Properties of NiCr-Re-Al<sub>2</sub>O<sub>3</sub> Coatings Deposited by HVOF, Atmospheric Plasma Spraying, and Laser Cladding. *J. Therm. Spray Technol.* **2022**, *31*, 1609–1633. [[CrossRef](#)]
29. Wang, L.; Yang, J.L.; Ni, J.X.; Liu, C.G.; Zhong, X.H.; Shao, F.; Zhao, H.; Tao, S.Y.; Wang, Y.H. Influence of Cracks in APS-TBCs on Stress Around TGO During Thermal Cycling: A Numerical Simulation Study. *Surf. Coat. Technol.* **2016**, *285*, 98–112. [[CrossRef](#)]
30. Sachinlal, A.; Nithin, P.; Krishnan, B. Nondestructive Evaluation of Aircraft Stealth Coating by Terahertz-Time Domain Spectroscopy: Experimental and Numerical Investigation. *Nondestruct. Test. Eval.* **2023**, *in press*. [[CrossRef](#)]
31. Zhong, H.; Xu, J.; Xie, X.L.; Yuan, T.; Reightler, R.; Madaras, E.I.; Zhang, X.C. Nondestructive Defect Identification with Terahertz Time-of-Flight Tomography. *IEEE Sens. J.* **2005**, *5*, 203–208. [[CrossRef](#)]
32. Xu, J.; Zhang, X. *Terahertz Science, Technology and Application*; Peking University Press: Beijing, China, 2007; pp. 69–70.
33. Tu, W.L.; Zhong, S.C.; Incecik, A.; Fu, X.B. Defect Feature Extraction of Marine Protective Coatings by Terahertz Pulsed Imaging. *Ocean Eng.* **2018**, *155*, 382–391. [[CrossRef](#)]

34. Niwa, M.; Hiraishi, Y.; Terada, K. Evaluation of Coating Properties of Enteric-Coated Tablets Using Terahertz Pulsed Imaging. *Pharm. Res.* **2014**, *31*, 2140–2151. [[CrossRef](#)]
35. Fukuchi, T.; Fuse, N.; Okada, M.; Fujii, T.; Mizuno, M.; Fukunaga, K. Measurement of Refractive Index and Thickness of Topcoat of Thermal Barrier Coating by Reflection Measurement of Terahertz Waves. *Electron. Commun. Jpn.* **2013**, *96*, 37–45. [[CrossRef](#)]
36. Ellingson, W.A.; Lipanovich, R.S.; Visher, R.J. Optical NDT Techniques for Ceramic Thermal Barrier Coatings. *Mater. Eval.* **2006**, *64*, 45–51.
37. Stifter, D. Beyond biomedicine: A review of alternative applications and developments for optical coherence tomography. *Appl. Phys. B* **2007**, *88*, 337–357. [[CrossRef](#)]
38. Mh, T.I.; Ruiz, R.D.; Huntley, J.M. Double-shot depth-resolved displacement field measurement using phase-contrast spectral optical coherence tomography. *Opt. Express* **2006**, *14*, 9643–9656.
39. Wei, Z.Y.; Cai, H.N.; Meng, G.H.; Tahir, A.; Zhang, W.W. An Innovative Model Coupling TGO growth and Crack Propagation for the Failure Assessment of Lamellar Structured Thermal Barrier Coatings. *Ceram. Int.* **2020**, *46*, 1532–1544. [[CrossRef](#)]
40. Unnikrishnakurup, S.; Dash, J.; Ray, S.; Pesala, B.; Balasubramaniam, K. Nondestructive Evaluation of Thermal Barrier Coating Thickness Degradation Using Pulsed IR Thermography and THz-TDS Measurements: A Comparative Study. *NDT E Int.* **2020**, *116*, 102367–102375. [[CrossRef](#)]

**Disclaimer/Publisher’s Note:** The statements, opinions and data contained in all publications are solely those of the individual author(s) and contributor(s) and not of MDPI and/or the editor(s). MDPI and/or the editor(s) disclaim responsibility for any injury to people or property resulting from any ideas, methods, instructions or products referred to in the content.